Research Article | Vol. 13, No. 8 / 1 Aug 2022 / Biomedical Optics Express 4190
Biomedical Optics EXPRESS

Label free optical transmission tomography for biosystems: intracellular structures and dynamics

VIACHESLAV MAZLIN,[1,3,*] OLIVIER THOUVENIN,[1,3] SAMER ALHADDAD,[1] MARTINE BOCCARA,[2] AND CLAUDE BOCCARA[1]

[1]Institut Langevin, ESPCI Paris, PSL University, CNRS, 1 rue Jussieu, 75005 Paris, France
[2]Institut de Systématique, Evolution, Biodiversité (ISYEB), Muséum National d'Histoire Naturelle, Sorbonne Université, EPHE, UA, CNRS ; CP 50, 57 rue Cuvier, 75005 Paris, France
[3]These authors contributed equally to this work
*mazlin.slava@gmail.com

Abstract: There is an increasing need for label free methods that could reveal intracellular structures and dynamics. In this context, we develop a new optical tomography method working in transmission - full-field optical transmission tomography (FF-OTT). The method can measure the forward scattering signals and reveals the time-dependent metabolic signals in living cells. FF-OTT is a common path interferometer taking advantage of the Gouy phase shift - a π phase shift that the light wave experiences around the focus. By modulating the position of the focus one can alter the phase of the scattered light. Demodulation of images with different phases rejects the background and enhances the light from the depth-of-field, thus producing an optical section. We test FF-OTT by imaging single-cell diatoms and ex vivo biological samples. In fresh samples, we show that the intracellular motions create visible intensity fluctuations in FF-OTT so that the method is able to reveal a metabolic dynamic contrast. FF-OTT was found to be an efficient label free technique that can be readily implemented thanks to a robust common-path speckle-free interferometer design using an incoherent light source.

1. Introduction

It is well-known that an object positioned outside of optical microscope focus stays visible and produces a blurred image. This presents a major problem for microscopy: image of interest from a thin depth-of-field slice can be completely hindered by the superimposed blurred background from the out-of-focus sample volume. With a goal to suppress the background and reveal only the relevant in-focus signals multiple techniques were developed. These are frequently referred to as 'optical sectioning' methods. These methods are numerous and show great diversity in physical and engineering principles that underlie them; therefore, we will restrain ourselves to the most common methods. Optical sectioning methods can be classified into general types: methods physically blocking the out-of-focus light before detection, like confocal microscopy [1], methods filtering the out-of-focus light in post-processing [2], light sheet methods illuminating a single in-focus plane perpendicular to the detection [3], structured illumination methods [4], phase contrast methods highlighting the refractive index changes [5,6], optical coherence tomography (OCT) methods that obtain cross-sectional [7] and en face sections [8] using the interference of light of low temporal coherence.

One of the earliest and the most widespread optical sectioning method is confocal microscopy (CM) [9], which uses a pinhole mask to physically block the out-of-focus light from reaching the detector. Interestingly, it was noticed that a further improvement in optical sectioning (and axial resolution) can be achieved by looking at the brightness of the scatterer [10]. More precisely, the visible intensity of the scatterer can be linearly correlated to its position by subtracting several

#453586 https://doi.org/10.1364/BOE.453586
Journal © 2022 Received 11 Jan 2022; revised 23 Apr 2022; accepted 5 May 2022; published 8 Jul 2022

Biomedical Optics EXPRESS

images along the point-spread-function (PSF) slope. This approach of optical profiling is called differential confocal microscopy (DSP) and can also be used in a two-camera configuration (one before and one after the focus) [11]. Differential spinning disk (DSD) [4,12] confocal microscopy is another method that relies on two image subtraction, however the images are different by the illumination patterns. Modern confocal systems use a combination of physical (block) and numerical filtering (image subtraction) to improve the background rejection and therefore the optical sectioning.

Although with a different principle, image subtraction is also used in full-field optical coherence tomography (FF-OCT) [8,13]. FF-OCT uses an interferometer coupled with a light source of low temporal coherence to produce interference between the reference light reflected from the mirror and backscattered light from a thin section of the sample. The phase of the interference is modulated by moving the reference mirror with a piezo-electric motor. Difference between the consecutive phase-shifted images doubles the interference signal and rejects the background thus producing an optical section. FF-OCT works directly in wide-field and does not require point-by-point scanning typical for confocal systems. Another particularity of FF-OCT and OCT techniques in general is that the thickness of the optical section is independent from the depth of field, and can be much smaller than the latter (determined by the spectral bandwidth of the light source). Many applications were found for FF-OCT including biopsy diagnostics [14], visualization of cell organoid dynamics [15,16], in vivo retinal [17] and corneal imaging [18].

Up to now FF-OCT was only used in a back-scattering configuration. In the majority of cases confocal microscopy uses a reflection configuration, although an elegant transmission geometry was also proposed [19].

Conversely, the optical phase contrast methods are primarily of transmission type. Transmission geometry natively enables interference between the light waves scattered by the sample and the waves transmitted without scattering (zero-order diffraction). By using one of the phase contrast techniques such as the classical one from Zernike [5,20], differential interference contrast (DIC) microscopy [21] or defocusing microscopy [22] it is possible to convert phase variations, caused by the light propagating through the thickness of the sample, into the intensity detectable by the camera. The resulting image provides a contrasted view of the sub-cellular structures, although the optical sectioning is modest.

In the current paper we introduce a new optical sectioning method that works in transmission. The method takes advantage of the Gouy phase shift [23] – the well-known π phase shift that the light wave experiences in the optical focus. The effect of Gouy phase shift modulating the interference signal of freely moving nanoparticles across the focus was shown using coherent [24] and incoherent light sources [25]. Here we study overall still samples, so, instead of relying on the random Brownian motion, we modulate the position of the focus using the piezo-electric motor. Hence, the phase of the scattered light oscillates causing a signal variation. Because the Gouy phase shift is localized at the focus of the objective, only the in-focus light is modulated while the out-of-focus light stays unchanged. Processing of images with different phases rejects the background and enhances the light from the depth-of-field, thus producing an optical section. In this way the optical sectioning is achieved by a combination of physical and numerical rejection of out-of-focus light (small depth-of-field of focusing optics combined with processing of phase-shifted images). In order to emphasize the transmission nature of the method and the fact that it works in full-field, we call it full-field optical transmission tomography (FF-OTT). We provide a basic theoretical framework for FF-OTT. Then we test its performance by imaging single-cell diatoms and ex vivo samples. Finally, we demonstrate the ability of FF-OTT to image the metabolic dynamic signals in living cells.

Biomedical Optics EXPRESS

2. Basic model of full-field optical transmission tomography

2.1. Principle of FF-OTT

The Gouy phase shift (GS) is a well-known π phase shift that a converging wave experiences as it passes through its focus. GS is a general property of all waves (light, sound, etc) and is applicable to any converging/diverging waveform [26]. Despite its widespread nature, the possible physical origins of GS were proposed only recently, rooting back to the fundamental uncertainty principle [27] and Huygens principle [28].

Phase changes are not visible to the conventional light detectors that measure intensity. However, one can convert phase variations into intensity variations using interference of the transmitted light wave with the wave scattered by the sample. The transmission interferometer is shown in Fig. 1. Light from the spatially incoherent source such as light-emitting diode (LED) is sent onto the sample. Part of the incoming wave is scattered by the sample and part is directly transmitted though the sample (zero order diffraction) without scattering. The transmitted wave passes through the microscope objective, focusing close to its back focal plane, and gets projected onto the camera by the tube lens. Conversely, the scattered wave is a diverging wave that is collected by the numerical aperture (NA) of the microscope objective, thus it exhibits the GS. The scattered wave gets focused on the camera and interferes with the transmitted light. In order to modulate the interference intensity of the scatterer and thus the location of the scatterer relatively to the focus, the microscope objective is mounted on the piezo-electric motor. Not every scatterer of the sample will exhibit sufficient GS, but only the scatterers within the DOF of the microscope objective (see the simulation below). By processing (typically, subtraction) the images corresponding to different phases, one can reject the out-of-focus background and recover the optical section – the so-called FF-OTT tomographic image. Below, FF-OTT is analyzed theoretically using a paraxial Gaussian beam approximation and experimentally by imaging nanoparticles.

2.2. Simulation and experiment with still nanoparticles

Basically, in our experiments the incoming wave illuminates the sub-wavelength scatterers such as the organelles in a cell volume generating a scattered field that is able to interfere with the incoming wave. We analyze the experiment using the Gaussian beam model that provides particularly simple equations.

The electric field of the scattered wave can be written as [29]:

$$E_S(r,z) = E_{S0} \cdot \frac{w_0}{w(z)} \cdot \exp\left(-\frac{r^2}{w^2(z)}\right) \cdot \exp\left(-i \cdot \left(k \cdot z + \underbrace{\frac{k \cdot r^2}{2 \cdot R(z)}}_{\text{Defocus}} - \underbrace{\arctan\left(\frac{z}{z_0}\right)}_{\text{Gouy shift}} - \frac{\pi}{2}\right)\right). \quad (1)$$

Here for simplicity we assumed an electric field with polarization in r direction and propagation in z direction. In the formula:

r is the lateral distance from the optical axis (r = 0 on the optical axis);

z is the axial distance from the optical focus (z = 0 at the focus);

$w(z) = w_0 \cdot \sqrt{1 + (z/z_0)^2}$ is the radius of the beam (depends on axial position z) ;

$w_0 = \lambda \cdot \sqrt{n^2 - NA^2}/(n \cdot \pi \cdot NA)$ is the beam waist radius at z = 0, that is computed by connecting divergence of the beam far from the waist $\theta = \lim_{z\to\infty} \arctan(w(z)/z) = \arctan(w_0/z_0) = \arctan(\lambda/(\pi \cdot w_0 \cdot n))$ [29] to the numerical aperture $NA = n \cdot \sin\theta$;

$z_0 = \pi \cdot {w_0}^2 \cdot n/\lambda$ is the Rayleigh length, essentially equivalent to half of the depth-of-field;

Biomedical Optics EXPRESS

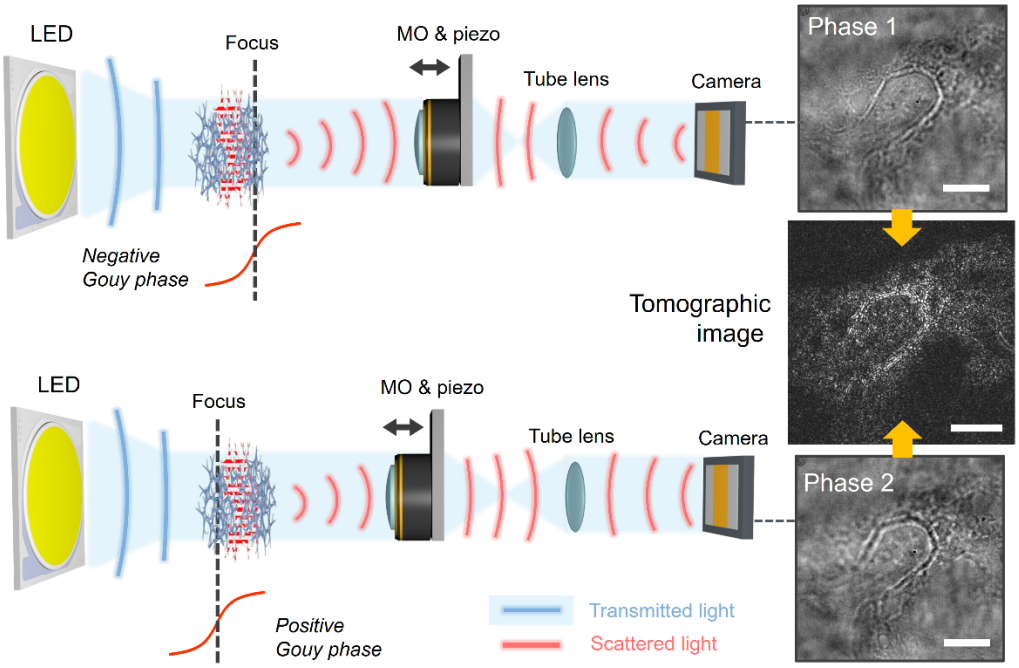

Fig. 1. Principle of FF-OTT: FF-OTT is based on interference of an illuminating wave and a wave scattered by the sample. Shifting position of the microscope objective (MO) modulates the Gouy phase of the scattered wave. Subtraction of the 2 phase shifted images removes the out-of-focus background, thus producing the tomographic image. Sample is a stromal keratocyte cell with visible nuclei from the ex vivo cornea. Scale bars are 10 µm.

E_{S0} is the amplitude of the electric field;
$R(z) = \frac{z^2 + z_0^2}{z}$ is the radius of curvature of the beam's wavefront at z;
$k = 2\pi n/\lambda$ is the wave number, λ is the wavelength and n is the refractive index of the medium;
$\pi/2$ is a phase shift due to scattering that is well-known in phase contrast microscopy [30].
On the optical axis at the center of the Gaussian beam ($r = 0$):

$$E_S(0,z) = E_{S0} \cdot \frac{w_0}{w(z)} \cdot \exp\left(- i \cdot \left(k \cdot z - \arctan\left(\frac{z}{z_0}\right) - \frac{\pi}{2}\right)\right) \tag{2}$$

At the same time, the transmitted wave propagating along the axis follows a simple plane-wave equation:

$$E_T(0,z) = E_{T0} \cdot \exp(- i \cdot k \cdot z) \tag{3}$$

The two fields interfere producing intensity detected by the camera:

$$I_{total} = |E_S|^2 + |E_T|^2 + 2 \cdot \mathrm{Re}\{ E_S \cdot E_T^*\} \tag{4}$$

The real interference term:

$$\mathrm{Re}\{E_S \cdot E_T^*\} = E_{S0} \cdot E_{T0} \cdot \frac{z/z_0}{1 + (z/z_0)^2} \tag{5}$$

Here we used a trigonometry relation. The relation between the interference term and axial position of the scatterer is plotted in Fig. 2(A).

Biomedical Optics EXPRESS

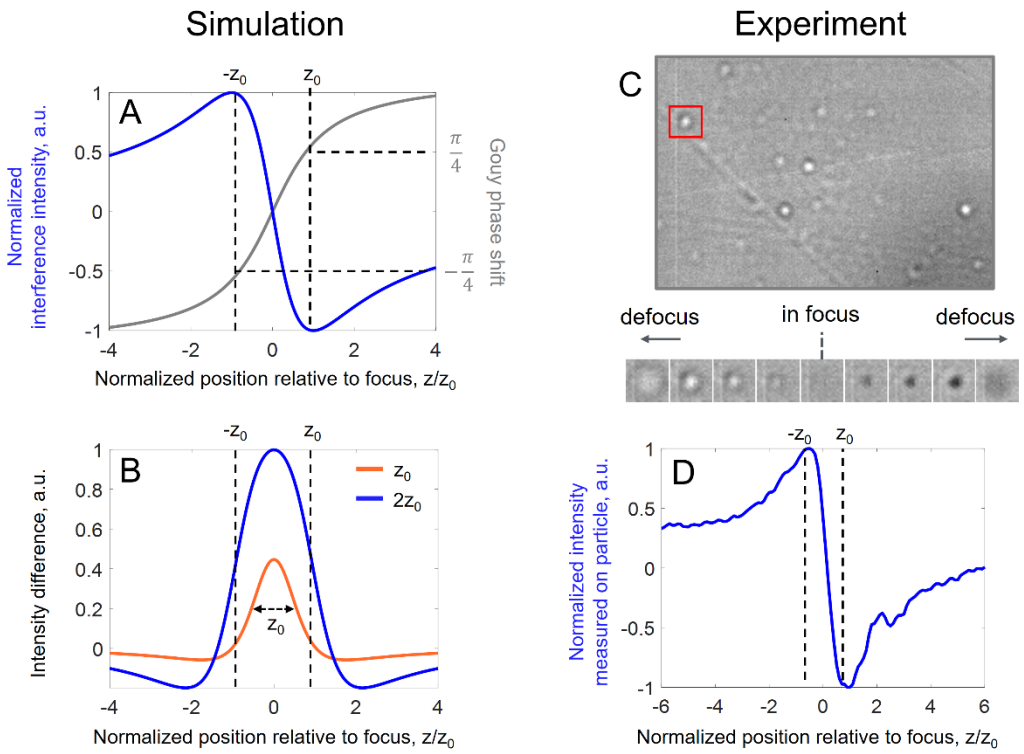

Fig. 2. FF-OTT simulation and experiment with nanoparticles. A: Gouy phase shift and its effect on the intensity of interference light in the focus. Depth-of-field (DOF) = $2 \times z_0 = 1.5$ µm. B: Optical sectioning effect depending on the phase step of the piezo motor. The curves are obtained by subtracting two phase-shifted blue curves in A. C: image on the camera with defocused nanoparticles visible. See the video in Visualization 1. D: Experimental change of nanoparticle intensity depending on the position relatively to the optical focus (generated from the Visualization 1).

In the case of a small scattering particle, the interference term is hindered by a strong homogeneous background, and the scattered intensity is negligible. The goal of FF-OTT is to remove the homogeneous background and isolate the interference term only. Close to the focus, where $z/z_0 << 1$ the expression of the interference term can be simplified:

$$\mathrm{Re}\{E_S \cdot E_T^*\} = E_{S0} \cdot E_{T0} \cdot \frac{z}{z_0} \tag{6}$$

Hence, around the focus the interference term changes the sign (for positive/negative z) and evolves linearly with the axial distance. This region of linear light intensity variation matches to the region of linear shift of Gouy phase. By subtracting the two camera frames, captured at different sides around the focus, we suppress the background light and double the in-focus interference term, thus achieving tomography. Change of focus between the two camera frames is typically done with a piezo motor holding the microscope objective.

$$I_{tomo} = I_{total1} - I_{total2} = E_{S0} \cdot E_{T0} \cdot \left[\frac{z + p/2}{z_0} - \frac{z - p/2}{z_0} \right] = E_{S0} \cdot E_{T0} \cdot \frac{p}{z_0} \tag{7}$$

with p being the piezo shift. Tomography can be achieved at different amplitudes of piezo modulation, however the highest signal from the tomographic section is reached, when the axial

Biomedical Optics EXPRESS

shift equals to depth-of-field ($2 \times z_0$), as seen in Fig. 2(A), B and [Eq. (7)]. For example, in 0.5 NA microscope system, this shift is about 1.5 µm. Depth-of-field (DOF) shift corresponds to $\pi/2$ change in Gouy phase that, being added to the $\pi/2$ phase of scattering [Eq. (2)], results in a total π phase shift of scattered light. Full width at half maximum of the blue curve in Fig. 2(B) gives the quantitative measure of axial resolution about $2 \times z_0 = \text{DOF}$. It is important to note that scattered light outside of the DOF is damped, however the damping is limited, when compared to OCT sectioning methods. Indeed, the sectioning in OCT (axial PSF) is usually linked to the Fourier transform of the close-to-Gaussian spectrum of the optical source and quickly converges to zero. Axial PSF of FF-OTT exhibits the non-negligible wings as seen in the blue curve of Fig. 2(B). This means that bright scatterers outside of DOF may be occasionally visible in the tomographic image. The signal from these scatterers can be further damped by reducing the piezo shift p below DOF to stay completely within the linear part of the phase shift. This also improves the axial resolution by two times reaching $z_0 = \text{half DOF}$ (orange curved in Fig. 2(B)). However, in this approach the tomographic signal is also reduced, which may prohibit imaging depending on the sensitivity of the optical system and of light scattering intensity from the sample.

As an experimental test for this model, we recorded an axial point-spread-function (PSF) of a small dielectric TiO_2 particle (diameter $< \lambda$). At the same time, the size was large enough (100 nm) to ensure the sufficient optical signal. The experiment used 100X oil immersion ($n_{oil} = 1.51$) microscope objective (AmScope, PA100X-INF-IRIS) with NA set to 0.5, resulting in the lateral resolution of $2 \times w_0 = 0.5$ µm and DOF of $2 \times z_0 = 1.5$ µm. The lateral resolution was greater than the particle size. The camera was oversampled (1 pixel corresponds to 0.07 µm), giving us the possibility to quantitatively explore the particle profile and brightness. The position of the objective was modulated with a piezo motor (NV 40/3 CLE, piezosystem Jena). Illumination from the blue (455nm) LED (M455L4, Thorlabs) was detected by the camera (PhotonFocus, MV-D1024E-160-CL-12) with high full well capacity of 200 000 e-. Results are shown in Figs. 2(C), 2(D) and in Visualization 1. One can see that intensity, and therefore the brightness of the particle, changes depending on whether it is located before or after the focus. At the same time the intensity of the background stays largely unchanged. By moving the piezo motor with 100 nm step we get an intensity curve on the particle that resembles the theoretical one in Fig. 2(A).

It is interesting to note that the effect of 'transparent objects showing light or dark contours under the microscope in different ways varying with change of focus' [5] was known long before Zernike used it to create a phase contrast microscope in the 1930s [20]. More recently this effect was used in electron microscopy [31] as well in optical microscopy of transparent homogeneous samples [22]. For such objects the wave curvature (defocus) was sufficient to explain the phase shift between the transmitted and scattered waves. Here, like in OCT, we explore objects that, due to their internal heterogeneous microstructures, scatter light. Our study suggests that for such micro-scattering objects the Gouy shift might also play a role in the phase contrast of these methods. For complex samples the intensity curve will result from the interplay of the Gouy and defocus effects.

3. Experimental results

3.1. Diatoms

Diatoms are single-cell algae that are of importance for environmental studies. An extended discussion about the biology of diatoms can be found in [32,33] and in the references therein. We used an experimental configuration similar to the one mentioned above. Phaeodactylum tricornutum CCMP632 was cultured in artificial sea water (40 g/L, Sigma) supplemented with f/2 nutrients and vitamins (F/2 Media Kit Bigelow NCMA) under continuous shaking (100 rpm) at 20 °C under cool white fluorescent lights (30 $\mu E.m^{-2}\ s^{-1}$) with a 12h photoperiod. For microscope observations we mixed the cells with melted 1% agar in culture medium and immediately

Biomedical Optics EXPRESS

observed them after jellification at room temperature. We have not applied environment control (no temperature and no CO_2 control), so that the temperature corresponds to room temperature (measured at ~22°C) and with low CO_2 concentration (~0.1% as in a normal closed environment). The diatoms are marine algae used to grow at ambient temperature (optimal temperature at 20°C) and low CO_2 concentration, close to the experimental conditions.

An optical slice can be retrieved by subtracting the two phase shifted images. Alternatively the objective can be moved sinusoidally, as in the integrated-bucket FF-OCT [34] in order to perform a lock in detection and increase the sensitivity to small scatterers. The focus shift in this test and in the corneal imaging experiment below was about 1 µm close to the DOF. Each image was acquired in 3 ms camera exposure time at 135 frames per second, resulting in 15 ms acquisition time for one tomographic frame. Results are shown in Fig. 3. FF-OTT suppresses the fuzzy background that is present in the direct camera images.

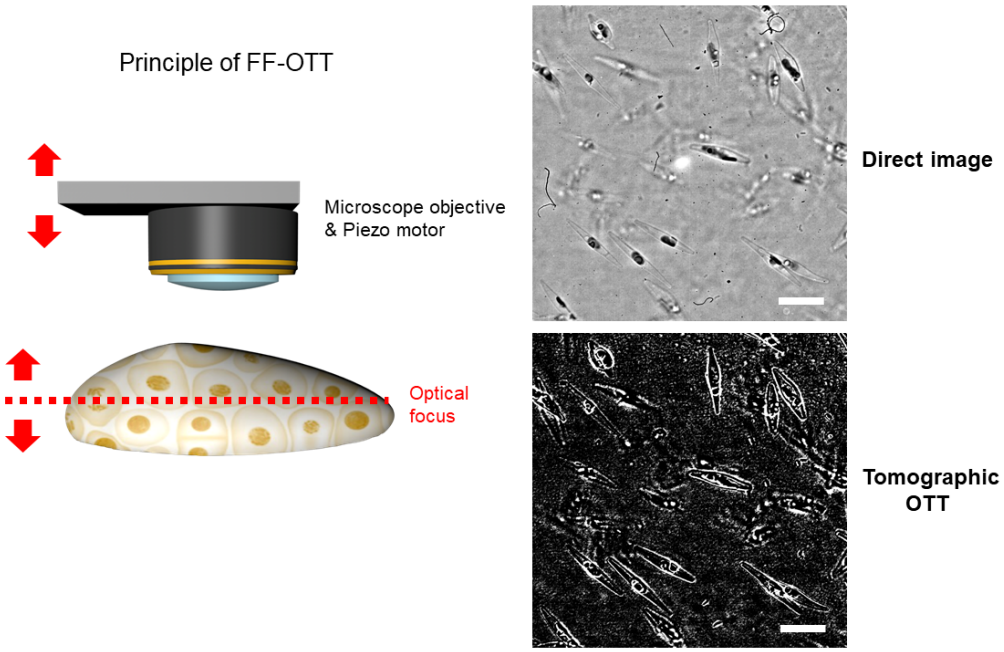

Fig. 3. FF-OTT in the study of diatoms. Direct image refers to a transmission image acquired by the camera without additional processing. Tomographic OTT image was reconstructed from two direct images shifted by about 1 µm. The scale bars are 15 µm.

3.2. *Ex vivo cornea*

Cornea is the most forefront transparent tissue that constitutes the eye. Its exploration is of great interest for medicine as it is a transplantable tissue. Multi-layer composition of the cornea makes its exploration with tomographic techniques particularly interesting and informative.

In order to explore the cell organization, we used an optical system with a smaller magnification but a larger frontal distance. The microscope objective was water immersion ($n_{water} = 1.33$) 60X NA = 1.1 (NA = 0.5 filled) (LUMFI, Olympus). The theoretical lateral and axial resolutions were 0.6 µm and 1.4 µm, while the FOV was about 180 µm. The samples - ex vivo porcine and macaque corneas were obtained from the partner research institution (Institut de la Vision, Paris) as recuperated waste tissue from an unrelated experiment. They were dissected from the ocular globes within the two hours post-mortem and were imaged within the same day using FF-OTT. In order to limit the spherical aberration due to refractive index mismatch between the sample

Biomedical Optics EXPRESS

and the water immersion as well as to make up for the degraded transparency of the sample over time, we first imaged the epithelium and stroma at the front and then flipped the cornea to view the endothelium and stroma at the back.

Corneal images revealed different structures including stromal keratocyte cells with nuclei (15 µm) and endothelial cell mosaic (20 µm) (Fig. 4). Curved endothelium overlapped with the flat focus plane (flat optical section) in a line, creating a visible intensity gradient. The stromal keratocyte cells and endothelial cells form single non-overlapping layers (axially). On the contrary epithelium is composed of dense 50 µm-thick cell mosaic layers that can obscure each other during imaging. Despite this complication FF-OTT was able to section through the epithelial sub-layer and reveal epithelial cells (40 µm) with nuclei (10 µm). The structures showed similar dimensions as visible in FF-OCT and confocal microscopy [18,35,36].

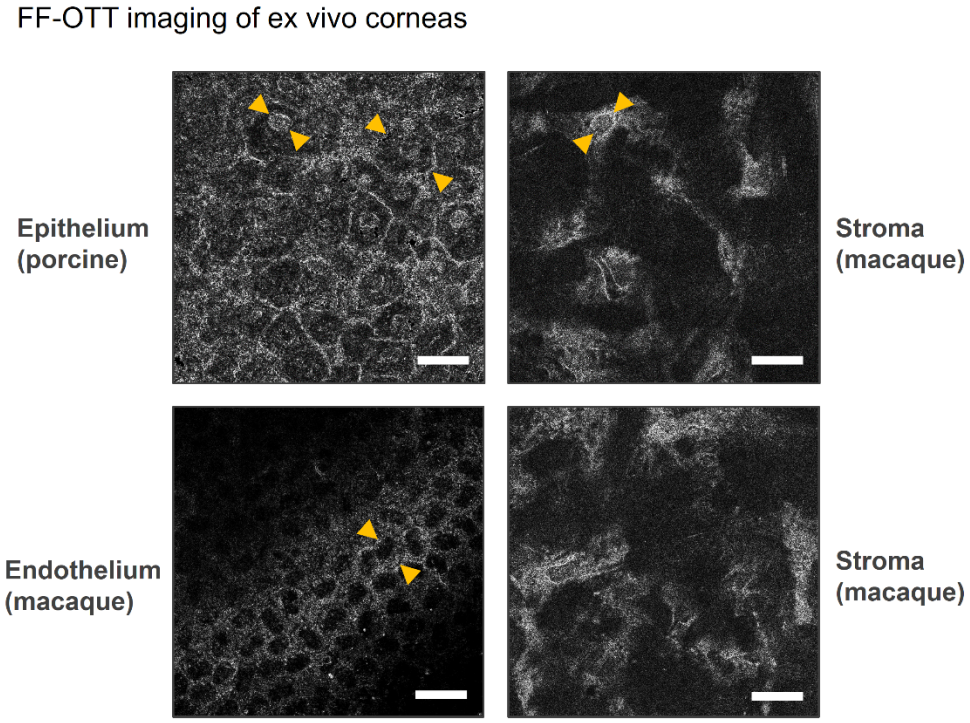

Fig. 4. FF-OTT images of ex vivo corneas. The stromal and endothelial images were acquired from the macaque cornea, while the epithelial image was taken from the porcine sample (epithelium in the macaque cornea was deteriorated). Arrows highlight the epithelial cell nuclei (10 µm), epithelial cell cytoplasm (40 µm), stromal keratocyte cell nuclei (15 µm) and endothelial cell (20 µm). Sectioning through videos are available as Visualization 2 and Visualization 3. Scale bars are 30 µm.

3.3. *Dynamic FF-OTT*

One peculiar feature of FF-OTT is that it can also be used to study the metabolic dynamics of the cells. In this context, instead of moving the microscope objective one can rely on the natural movements of the sub-cellular organelles. Thanks to the linearity of the axial interferometric response in FF-OTT, the axial displacements of the live scatterers inside the cell are transferred into the intensity differences. The intensity fluctuation images contain information that can be used to compute the optical section as before, but also contain information to evaluate the active

Biomedical Optics EXPRESS

transport of the scatterers inside the cell. Because the intensity strongly depends on the axial response only around the focal plane, the dynamic FF-OTT signal also exhibits optical sectioning. As such this method is a transmission analog of another label free method - dynamic FF-OCT that is being used in back-scattering [15,16].

An extended analysis of dynamic FF-OTT application to diatoms can be found in a biology-oriented paper [32,33], while in this work we demonstrate the promise of the method for imaging 2D cell cultures and 3D retinal layers.

We first illustrate the dynamic FF-OTT method by studying the behavior of HeLa cells (93021013-1VL, Merck) [37] grown on a cover slip in a Petri dish. The cells were positioned in the best focus of the FF-OTT device. Here we used a high resolution 100X oil immersion FF-OTT device mentioned above. We acquired a time stack of 256 consecutive camera frames at 100 frames per second. The piezo motor was static during acquisition and only the internal movements of the organelles were responsible for the phase changes. After the 3-D acquisition, the stack was processed to form the corresponding HSV colored dynamic image that recapitulates the local fluctuations (Fig. 5). This color image is based upon the 3 following independent channels:

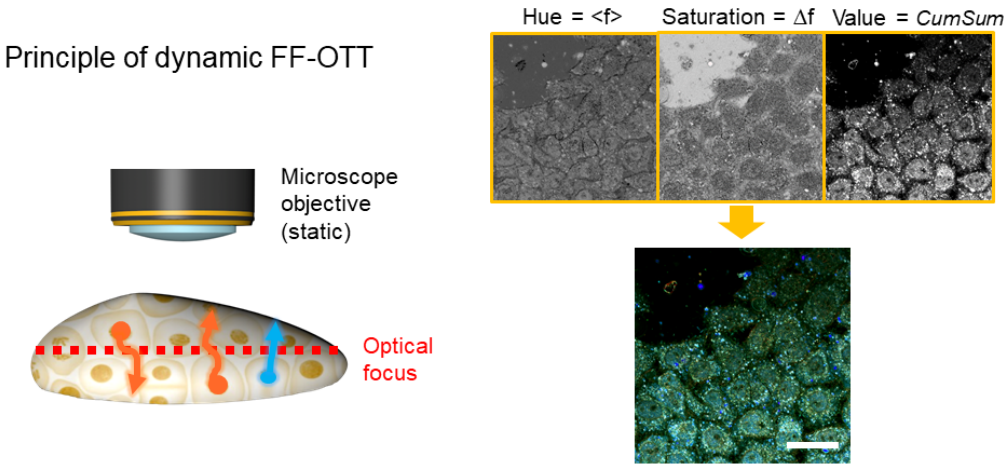

Fig. 5. Dynamic FF-OTT principle. Instead of moving the optical focus, one can rely on natural movements of sub-cellular organelles around the optical focus for phase shifting. The stack of 256 direct images contains sufficient information to reconstruct a tomographic image with the cell metabolism encoded in the color (blue = slow, red = fast). This is done by looking at the time evolution of each pixel of the stack and by measuring the average frequency of modulation, frequency range Δf and cumulative sum (CumSum). Then HSV image is created by assigning these parameters to each channel. Scale bar is 20 µm.

- Hue, or central color, measures the central fluctuation frequency (how fast does the signal fluctuate). For each pixel, the absolute value of the Fourier transform of the normalized time series is calculated. The cumulative distribution of half the spectrum is calculated and the median value defines the hue of the corresponding pixel. The obtained values are reverted and normalized between 0 and 0.66 (with 1% saturation) so that high frequencies (fast fluctuations due to moving organelles) appear red, and low frequencies (slow fluctuations) appear blue.

- Saturation, or the purity of each color, measures the frequency range. The 25th and 75th percentiles from the previous distribution are measured to extract the frequency bandwidth (in which 50% of the energy of the fluctuation is). The obtained values are reverted and normalized between 0 and 1 (with 1% saturation) so that large bandwidths (typical noise) appear with a low saturation and narrow frequency bandwidth appear more contrasted.

Biomedical Optics EXPRESS

- Value, or brightness of each color, measures the amplitude of fluctuations (how much does the signal fluctuate). In practice, we subtract the mean value of time series, and divide it into 16 buckets of 16 images, corresponding to 160 ms. The absolute value of the maximum value of the cumulative sum in each bucket is calculated, and the sum of these 16 values finally gives the value of the corresponding pixel. This *cumsum* strategy was shown to be more efficient for detecting small uniaxial displacements versus a random noise as standard deviation [38]. The obtained values are normalized between 0 and 1 (with 1% saturation), so that large fluctuations appear brighter than small fluctuations.

In order to confirm that the color signal originates from the cell metabolism we applied on the sample the D-oxy-glucose that inhibits glycolysis and stops part of the energy supply [39]. The D-oxy-glucose was added to the solution by mechanical pipetting so that the final concentration of D-oxy-glucose reached 10 mM. After this addition, cells were put back to the incubator (37°C, 5% CO_2) for 20 minutes before imaging at 3 time points (20 min, 1 h, 2 h). They were also compared to control cells, to which we added the same quantity of culture medium (instead of the D-oxy-glucose solution). Both control and D-oxy-glucose affected cells were imaged without temperature or CO_2 control. Although cells would benefit from a controlled environment (typically 37°C, 5% CO_2, mostly important to control pH on long timescales), implementing micro-incubator was too expensive at this stage of the demonstration. Moreover, in the previous paper on dynamic FF-OCT [40], we showed that the main difference between room temperature and 37°C (and supplied medium to control pH) was a slight increase in the frequency range of fluctuations inside the cytoplasm, far below what was observed. Conversely, D-oxy-glucose is known to produce strong effects on dynamic FF-OCT signal [15]. Although long term pH changes (if CO_2 is not at 5%) could induce cell apoptosis, we have seen that this happens on large timescales, and we can usually detect dynamic signals in cultured cells in non-controlled conditions for several hours without critical change. Nevertheless, micro-incubator would be required for a detailed investigation of drug effects on cell metabolism in the future.

The evolution of dynamic FF-OTT images is shown in Fig. 6. As expected the cytoplasm signal decreases in time [38].We also noticed a 2 to 5 times increase in dynamic signal from the nuclei. In order to better characterize these dynamics we compared the standard deviation and the cumulative sum, following the method developed by Scholler [38]. We found that the normalized cumulative sum was about the same as the standard deviation (ratio 1.3) before the addition of the D-oxy-glucose and it increased to a ratio of 2.5 after the addition. This result suggests that the random movement of scatterers within the nuclei is likely to be associated to a drift that makes it anomalous, rather than being a pure Brownian motion. Indeed, anomalous movements have been already described in the nucleus and D-oxy-glucose has been shown to inhibit protein transport from the cytoplasm to nucleus [41,42].

Dynamic FF-OTT can be performed not only in cell cultures, but also in thick samples like ex vivo pig retina. The results are shown in Visualization 4. The ex vivo pig retina was obtained from the partner research institution (Institut de la Vision, Paris) as recuperated waste tissue from a regional slaughterhouse. The retina was dissected from the ocular globe within two hours post-mortem and was imaged within the same day using FF-OTT. The tissue was put on a simple coverslip and was immerged in PBS. The drift in the liquid was causing occasional motion artifacts in the images. The light traveled through the full thickness of the retina, while the ganglion cell layer, close to the surface of the retina was imaged. 256 images were acquired at each plane, separated by 2 µm, and one dynamic FF-OTT image was calculated at each plane. The direct intensity image, the static FF-OTT and the dynamic FF-OTT images were combined together in Visualization 4. The first layer of flat and large cells, possibly glial cells is visible in dynamic FF-OTT, followed by a few planes, where large and small circular ganglion cells as well as their nuclei can be observed together with large axons in static FF-OTT. The retinal ganglion cells exhibit smaller amplitude but faster dynamics as compared to the first class of (blue) cells.

Biomedical Optics EXPRESS

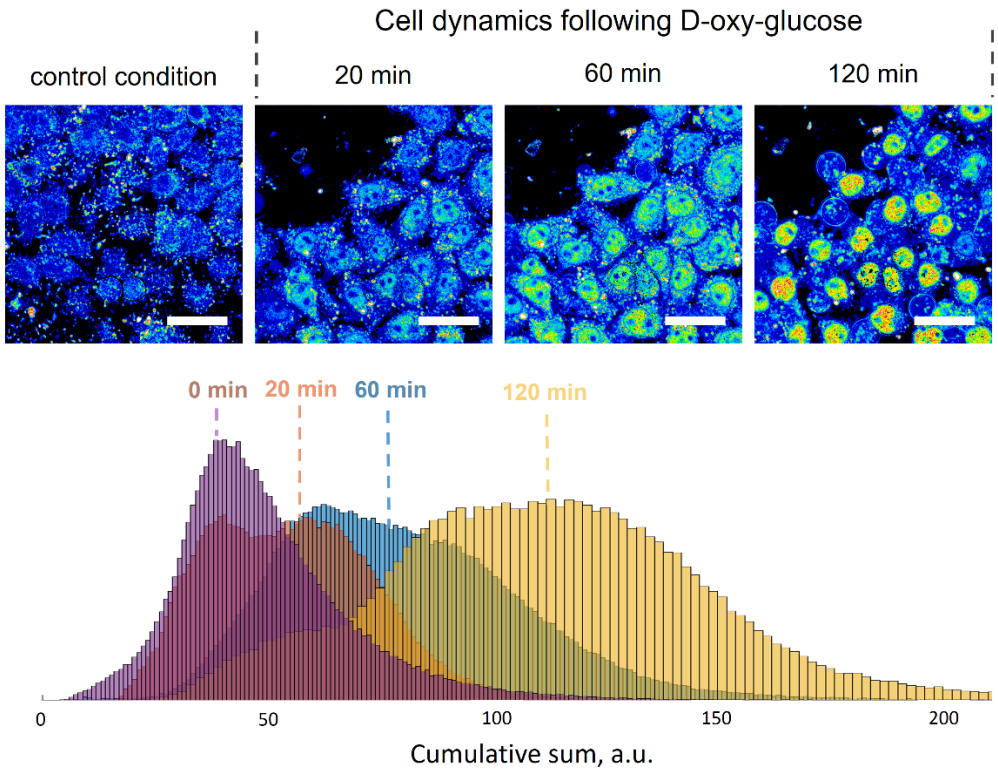

Fig. 6. Dynamic FF-OTT application to imaging HeLa cell metabolism. Introduction of D-oxy-glucose partly blocks the cell energy supply resulting in the expected reduced dynamic signal from the cytoplasm and increased signal from the nuclei, as seen by FF-OTT. Histogram is calculated by measuring the cumulative sum signal at each pixel within the nuclei. The method did not require any fluorescent biomarkers. Scale bars are 20 µm.

Finally, the inner plexiform layer with many point-like synapses was visible, together with the first few bipolar cells from the inner nuclear layer. Altogether, many different cells and features of the retina can be investigated by combining static and dynamic FF-OTT.

It is important to mention the range of movement frequencies that can be investigated with dynamic FF-OTT. The maximal measurable frequency is half the acquisition frequency (about 100 frames per second maximum with the current camera). The minimal frequency is the ratio between the acquisition frequency and the number of frames acquired. In the case of HeLa cells, it corresponds to 100/256 ~ 0.4 Hz. Smaller frequencies could be obtained by either reducing the acquisition frequency, or by increasing the number of acquired frames. Based on our own experience of FF-OCT, most cellular processes that we can track are in the 1–10 Hz frequency range. At low frequencies below 1 Hz the mechanical and thermal noise perturb the signals, while high frequency changes above 50 Hz are rarely detectable in small moving cellular organelles. Note that the quantitative interpretation of the measured frequencies is complicated because it depends on both the biological process itself and the actual speed of the object, but also on the signal level and phase sensitivity of the system as well as on the size of the scatterer.

4. Discussion, conclusion and perspectives

FF-OTT introduces a new optical sectioning method that exploits the effect of Gouy phase shift. The optical sectioning of about depth-of-field is achieved by a combination of the physical (high

Biomedical Optics EXPRESS

numerical aperture) and numerical (phase shifting) rejection of out-of-focus light. One of the main advantages of the method is the particularly simple setup. The common-path interferometer design with a single microscope objective does not require high precision mechanics and is immune to mechanical/thermal misaligning. FF-OTT can be used to get a distribution of microorganisms (e.g. algae) and to section through ex vivo samples. The method is particularly interesting for imaging ex vivo cornea samples, as it shows similar features as FF-OCT and confocal microscopy, while using a much simpler device. As such, FF-OTT is promising for diagnostics of corneal grafts.

Compared to FF-OCT, the axial resolution in the new method is determined by the numerical aperture of the optics used and not the spectral bandwidth of the light source, which limits FF-OTT to the use of relatively high-NA objectives. Another distinctive feature of FF-OTT is that it uses a common-path interferometer, which eliminates the problem of mismatch between the optical focus and the coherence plane present in FF-OCT [43]. However, the lack of an independent reference arm means that both the sample and reference signals are getting damped, when propagating through thick strongly absorbing or scattering media. Part of this disadvantage is compensated by the fact that biological tissues are mostly "forward scatterers" due to the size of cells and nuclei (scattering by the structures larger than hundred nanometers is highly anisotropic in the forward direction). Lastly, in contrast to FF-OCT the new method does not produce the optical interference fringe artifacts typically observed in cells cultures on glass or plastic slides, or in regular cell mosaics, such as corneal endothelium [44].

The most peculiar feature of FF-OTT is its ability to visualize the metabolic cell dynamics without fluorescent labels. In this sense, FF-OTT can produce images similar to the dynamic backscattering-based FF-OCT [15,16], while using a much simpler and robust optical design.

Among the limitations of the method, we should mention the finite damping of the out-of-focus light (see the wings of the curve in Fig. 2(B)), when compared to the strong interferometric damping in OCT. Indeed, the OCT sectioning (axial PSF) is usually linked to the Fourier transform of the close to Gaussian source spectrum and quickly converges to zero. For FF-OTT, as could be seen on Fig. 2(B), we need to use an axial modulation smaller than the depth of field to get acceptable damping of the axial PSF wings. However, in this approach the tomographic signal is also reduced, which may prohibit imaging depending on the sensitivity of the optical system and of light scattering intensity from the sample.

It is important to note that the thickness and scattering of the tissue under examination affect FF-OTT imaging, moreover the impact is different from the tissue volumes located before and after the FF-OTT imaging plane. Light that is getting scattered between the source and the imaging plane is acting as a secondary illumination source for the sample. This leads to an equivalent FF-OTT device with the source located closer to the sample The imaging quality is preserved under the modest requirement that the thickness, scattering and absorption are limited so that a sufficient amount of light can still reach the imaging plane of the sample, can be captured by the NA of the microscope objective and can generate a "reference" signal much larger than the scattered signal of interest. On the other hand, the requirement for the tissue volume located between the imaging plane and microscope objective is stricter. Given that FF-OTT is interferometric method (like OCT), the useful signal is composed of ballistic single scattering photons that are getting exponentially damped through the tissue. The damping limits the accessible imaging depth to the mean free path. The latter is relatively short about 100 µm in biological samples but can reach 1 mm in transparent tissues like the cornea. One advantage of the transmission-based FF-OTT compared to reflection-based OCT is that light propagates only once through the tissue, therefore the mean free path required for imaging can be twice shorter.

Although our simple theoretical model shows agreement with the experiment, the understanding of FF-OTT would greatly benefit from a more rigorous theoretical analysis in the future. This model should take into account the high-NA optics (not completely valid for Gaussian beams) as

Biomedical Optics EXPRESS

well as the different numerical apertures for the transmitted and scattered waves. More precisely, the NA of the transmitted beam is determined by the LED illumination angle, while the NA of the scattered wave depends on the size of the scatterers. Finally, the scattering from the real samples is complex - even the scattering electric field from the 100 nm particles is located in a larger region than the particle itself. The angular distribution as well as the geometrical parameters of the scattered electric field should be taken into account.

Funding. Agence Nationale de la Recherche (ANR-10-IDEX-0001-02 PSL, PRIMAVERA); Horizon 2020 Framework Programme (754387); European Research Council (957546).

Acknowledgments. We warmly thank Morgane Corre from IBENS for the HeLa cells cultures on glass slides that we used in this study, as well as Valérie Fradot for preparing the corneal samples.

Disclosures. OT: (P), MB: (P), ACB (P), SA: none, VM: none.

Data availability. Full resolution images generated in this paper are not publicly available at this time but may be obtained from the authors upon reasonable request.

References

1. J.-A. Conchello and J. W. Lichtman, "Optical sectioning microscopy," Nat Methods **2**(12), 920–931 (2005).
2. W. Wallace, L. H. Schaefer, and J. R. Swedlow, "A workingperson's guide to deconvolution in light microscopy," BioTechniques **31**(5), 1076–1097 (2001).
3. J. M. Girkin and M. T. Carvalho, "The light-sheet microscopy revolution," J. Opt. **20**(5), 053002 (2018).
4. J. Mertz, "Optical sectioning microscopy with planar or structured illumination," Nat Methods **8**(10), 811–819 (2011).
5. F. Zernike, "How I discovered phase contrast," Science **121**(3141), 345–349 (1955).
6. . "Optical Sectioning with Phase Contrast and DIC - Java Tutorial | Olympus LS," https://www.olympus-lifescience.com/en/microscope-resource/primer/java/dic/dicphaseos/.
7. D. Huang, E. A. Swanson, C. P. Lin, J. S. Schuman, W. G. Stinson, W. Chang, M. R. Hee, T. Flotte, K. Gregory, C. A. Puliafito, and J. G. Fujimoto, "Optical coherence tomography," Science **254**(5035), 1178–1181 (1991).
8. E. Beaurepaire, A. C. Boccara, M. Lebec, L. Blanchot, and H. Saint-Jalmes, "Full-field optical coherence microscopy," Opt. Lett. **23**(4), 244–246 (1998).
9. M. Minsky, "Memoir on inventing the confocal scanning microscope: Memoir on Inventing the confocal scanning microscope," Scanning **10**(4), 128–138 (1988).
10. C.-H. Lee and J. Wang, "Noninterferometric differential confocal microscopy with 2-nm depth resolution," Opt. Commun. **135**(4-6), 233–237 (1997).
11. J. Tan and F. Wang, "Theoretical analysis and property study of optical focus detection based on differential confocal microscopy," Meas. Sci. Technol. **13**(8), 1289–1293 (2002).
12. . "Revolution DSD - Andor Learning Centre," https://andor.oxinst.com/learning/view/article/revolution-dsd.
13. A. Dubois, *Handbook of Full-Field Optical Coherence Microscopy: Technology and Applications* (Routledge, 2016).
14. O. Thouvenin, C. Apelian, A. Nahas, M. Fink, and C. Boccara, "Full-field optical coherence tomography as a diagnosis tool: recent progress with multimodal imaging," Appl. Sci. **7**(3), 236 (2017).
15. C. Apelian, F. Harms, O. Thouvenin, and A. C. Boccara, "Dynamic full field optical coherence tomography: subcellular metabolic contrast revealed in tissues by interferometric signals temporal analysis," Biomed. Opt. Express **7**(4), 1511 (2016).
16. J. Scholler, K. Groux, O. Goureau, J.-A. Sahel, M. Fink, S. Reichman, C. Boccara, and K. Grieve, "Dynamic full-field optical coherence tomography: 3D live-imaging of retinal organoids," Light Sci. Appl. **9**(1), 140 (2020).
17. P. Mecê, J. Scholler, K. Groux, and C. Boccara, "High-resolution in-vivo human retinal imaging using full-field OCT with optical stabilization of axial motion," Biomed. Opt. Express **11**(1), 492 (2020).
18. V. Mazlin, P. Xiao, J. Scholler, K. Irsch, K. Grieve, M. Fink, and A. C. Boccara, "Real-time non-contact cellular imaging and angiography of human cornea and limbus with common-path full-field/SD OCT," Nat. Commun. **11**(1), 1868 (2020).
19. C. Yang and J. Mertz, "Transmission confocal laser scanning microscopy with a virtual pinhole based on nonlinear detection," Opt. Lett. **28**(4), 224 (2003).
20. F. Zernike, "Phase contrast, a new method for the microscopic observation of transparent objects," Physica **9**(7), 686–698 (1942).
21. L. Walter, *Nomarski Differential Interference-contrast Microscopy* (Carl Zeiss, 1982).
22. U. Agero, L. G. Mesquita, B. R. A. Neves, R. T. Gazzinelli, and O. N. Mesquita, "Defocusing microscopy," Microsc. Res. Tech. **65**(3), 159–165 (2004).
23. L. G. Gouy, "*Sur une propriété nouvelle des ondes lumineuses*," C. R. Acad. Sci. Paris, 1251 (1890).
24. J. Hwang and W. E. Moerner, "Interferometry of a single nanoparticle using the Gouy phase of a focused laser beam," Opt. Commun. **280**(2), 487–491 (2007).

Biomedical Optics EXPRESS

25. M. Boccara, Y. Fedala, C. V. Bryan, M. Bailly-Bechet, C. Bowler, and A. C. Boccara, "Full-field interferometry for counting and differentiating aquatic biotic nanoparticles: from laboratory to Tara Oceans," Biomed. Opt. Express **7**(9), 3736 (2016).
26. A. E. Siegman, *Lasers* (Univ. Science books, 1986).
27. S. Feng and H. G. Winful, "Physical origin of the Gouy phase shift," Opt. Lett. **26**(8), 485 (2001).
28. T. Lee, Y. Cheong, H. W. Baac, and L. J. Guo, "Origin of Gouy Phase Shift Identified by Laser-Generated Focused Ultrasound," ACS Photonics **7**(11), 3236–3245 (2020).
29. O. Svelto, *Principles of Lasers* (Springer US, 2010).
30. Y. Park, C. Depeursinge, and G. Popescu, "Quantitative phase imaging in biomedicine," Nature Photon **12**(10), 578–589 (2018).
31. K. Nagayama, "Phase contrast electron microscopy," in *Encyclopedia of Biophysics*, G. C. K. Roberts, ed. (Springer Berlin Heidelberg, 2013), pp. 1837–1841.
32. H. Bey, F. Charton, H. C. de Carvalho, S. Liu, R. G. Dorrell, C. Bowler, C. Boccara, and M. Boccara, "Dynamic cell imaging: application to the diatom phaeodactylum tricornutum under environmental stresses (bioRxiv 2021.10.22.465453, 2021).
33. H. Bey, F. Charton, H. C. de Carvalho, S. Liu, R. G. Dorrell, C. Bowler, C. Boccara, and M. Boccara, "Dynamic cell imaging: application to the diatom phaeodactylum tricornutum under environmental stresses," European Journal of Phycology (accepted) (2022).
34. A. Dubois, L. Vabre, A.-C. Boccara, and E. Beaurepaire, "High-resolution full-field optical coherence tomography with a Linnik microscope," Appl. Opt. **41**(4), 805 (2002).
35. V. Mazlin, P. Xiao, E. Dalimier, K. Grieve, K. Irsch, J.-A. Sahel, M. Fink, and A. C. Boccara, "In vivo high resolution human corneal imaging using full-field optical coherence tomography," Biomed. Opt. Express **9**(2), 557–568 (2018).
36. R. F. Guthoff, A. Zhivov, and O. Stachs, "*In vivo* confocal microscopy, an inner vision of the cornea - a major review," Clinical & Experimental Ophthalmology **37**(1), 100–117 (2009).
37. J. R. Masters, "HeLa cells 50 years on: the good, the bad and the ugly," Nat Rev Cancer **2**(4), 315–319 (2002).
38. J. Scholler, "Motion artifact removal and signal enhancement to achieve in vivo dynamic full field OCT," Opt. Express **27**(14), 19562 (2019).
39. T. Nguyen and O. Bensaude, "Increased thermal aggregation of proteins in ATP-depleted mammalian cells," Eur J Biochem **220**(1), 239–246 (1994).
40. C.-E. Leroux, F. Bertillot, O. Thouvenin, and A.-C. Boccara, "Intracellular dynamics measurements with full field optical coherence tomography suggest hindering effect of actomyosin contractility on organelle transport," Biomed. Opt. Express **7**(11), 4501 (2016).
41. I. Bronshtein, E. Kepten, I. Kanter, S. Berezin, M. Lindner, A. B. Redwood, S. Mai, S. Gonzalo, R. Foisner, Y. Shav-Tal, and Y. Garini, "Loss of lamin A function increases chromatin dynamics in the nuclear interior," Nat Commun **6**(1), 8044 (2015).
42. A. Zidovska, D. A. Weitz, and T. J. Mitchison, "Micron-scale coherence in interphase chromatin dynamics," Proc. Natl. Acad. Sci. **110**(39), 15555–15560 (2013).
43. S. Labiau, G. David, S. Gigan, and A. C. Boccara, "Defocus test and defocus correction in full-field optical coherence tomography," Opt. Lett. **34**(10), 1576 (2009).
44. V. Mazlin, K. Irsch, K. Irsch, M. Paques, J.-A. Sahel, J.-A. Sahel, J.-A. Sahel, M. Fink, and C. A. Boccara, "Curved-field optical coherence tomography: large-field imaging of human corneal cells and nerves," Optica **7**(8), 872–880 (2020).